ACS OMEGA

Open Access

http://pubs.acs.org/journal/acsodf

Article

Structure-Based Engineering of Monoclonal Antibodies for Improved Binding to Counteract the Effects of Fentanyl and Carfentanil

Justas Rodarte,[⊥] Carly Baehr,[⊥] Dustin Hicks, Morgan McGovern, Yue Zhang, Pedro Silva-Ortiz, Bryan Hannon, Sowmya Duddu, Marie Pancera,* and Marco Pravetoni*

Cite This: *ACS Omega* 2024, 9, 42506−42519

Read Online

ACCESS | Metrics & More | Article Recommendations | Supporting Information

ABSTRACT: The opioid overdose epidemic is a growing and evolving public health crisis fueled by the widespread presence of fentanyl and fentanyl analogues (F/FAs) in both street mixtures and counterfeit pills. To expand current treatment options, drug-targeting monoclonal antibodies (mAbs) offer a viable therapeutic for both pre- and postexposure clinical scenarios. This study reports the isolation, *in vitro* characterization, and *in vivo* efficacy of two murine mAb families targeting fentanyl, carfentanil, or both. Because humanization of the mAbs by CDR grafting negatively impacted affinity for both fentanyl and carfentanil, crystal structures of mAbs in complex with fentanyl or carfentanil were analyzed to identify key residues involved in ligand binding in murine versus humanized structures, and site-directed mutagenesis was used to verify their functional importance. The structural analysis identified a framework residue, Tyr36, present in the murine germline sequence of two mAbs, which was critical for binding to fentanyl and carfentanil. These studies emphasize the importance of structural considerations in mAb engineering to optimize mAbs targeting small molecules including opioids and other drugs of public health interest.

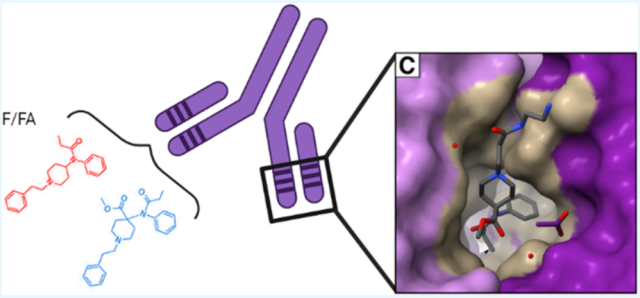

INTRODUCTION

Treatment of opioid use disorder (OUD) and overdose is a complex medical task involving orthogonal approaches, including medication-assisted treatment (MAT), behavioral therapy, and counseling in inpatient and outpatient settings. During the COVID-19 pandemic, increases in social isolation and emotional stress led to an increase in the prevalence of substance use disorders (SUDs) and overdoses, especially those involving synthetic opioids.[1] In response, health agencies endorsed remote treatments, such as telehealth therapy and remote group therapy, while also increasing opioid drug allowances.[2,3] Although these policies fostered high compliance and treatment outcomes remained positive,[2] opioid overdose deaths showed no abatement in 2021 or 2022.[4] While recent statistics show a small decline, the persistence of overdose deaths suggests that these temporary factors have resulted in permanent increases in opioid use. Presently, the opioid overdose epidemic is partly driven by the widespread prevalence of fentanyl and fentanyl analogues (F/FA), which can be encountered alone or in combination with other drugs in street mixtures or counterfeit pills.[5] Further, the OUD and overdose crisis disproportionately affects marginalized and minority communities;[6,7] due to systemic inequalities, biases in the medical community, and stigma associated with opioid agonists used in medication-assisted treatment (MAT), these populations are less likely to both seek and receive treatment, reducing the clinical impact of available therapies.[6,7] Hence, a broader range of treatment options to serve a diverse patient population is needed to combat the ever-evolving epidemic.

MAT for OUD includes pharmacotherapies such as mu-opioid receptor (MOR) agonists (methadone), partial agonists (buprenorphine), antagonists (naltrexone), combination therapies (Suboxone, buprenorphine/naloxone),[8] or extended-release formulations (e.g., Vivitrol or Probuphine). These are daily or monthly prescription treatments delivered in addition to behavioral treatments during or following the cessation of regular illicit drug use. For treatment of overdose, while naloxone (e.g., Narcan) has been the only approved drug for treating opioid overdoses since 1971,[9] the FDA approved the longer-acting nalmefene in 2023. However, there are limits to patient compliance with medication regimens and behavioral therapy for OUD. Even with methadone or buprenorphine

Received: July 17, 2024
Revised: August 22, 2024
Accepted: September 23, 2024
Published: October 7, 2024

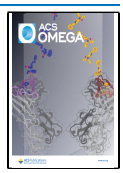

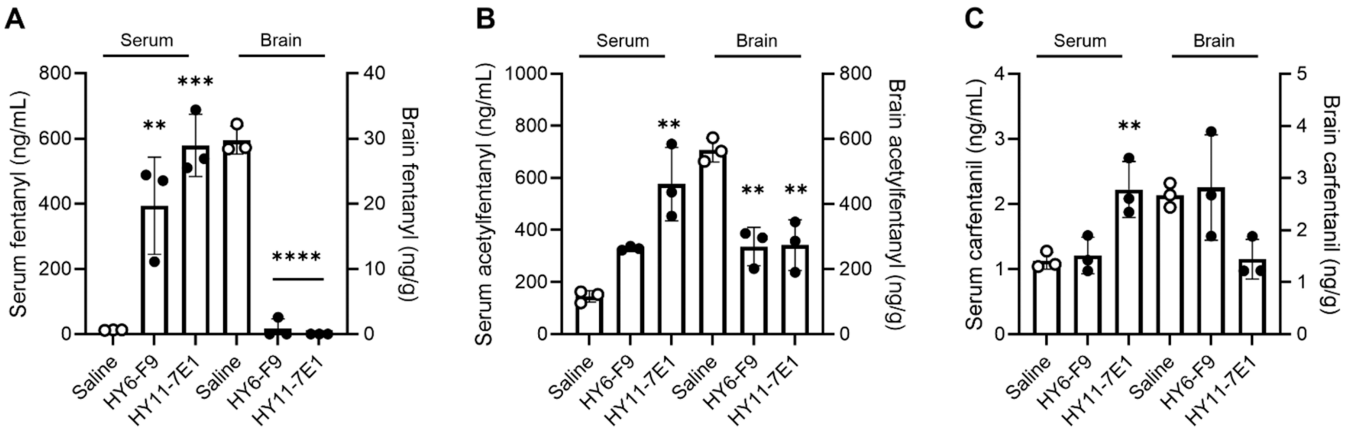

Figure 1. Efficacy of fentanyl-specific mAbs against F/FA in mice. Mice were passively immunized with 40 mg/kg murine HY6-F9 or HY11-7E1 and challenged with 0.1 mg/kg fentanyl, 1.0 mg/kg acetylfentanyl, or 0.02 mg/kg carfentanil 24 h after passive immunization. Concentrations of (A) fentanyl, (B) acetylfentanyl, or (C) carfentanil in serum (left *y*-axis) and the brain (right *y*-axis) were measured 30 min after drug administration. $^{**}p < 0.01$, $^{***}p < 0.001$, $^{****}p < 0.0001$ compared to saline control.

treatment, relapse rates at 6 months can be up to 50%, suggesting that interventions that function on longer time scales are necessary.[10] The high potency and long half-life of F/FA make relapse more dangerous and complicate overdose reversal by requiring multiple naloxone doses over a longer time.[11] The increase in the potency and availability of opioids over the last 10 years of the OUD epidemic, from oxycodone to illicit drugs containing F/FA, puts people at higher risk for exposure to deadly drug doses. Hence, the development of new treatments for OUD and overdose remains a public health priority.

In addition to the increased availability of existing F/FA, new psychoactive substances (NPSs) continue to emerge worldwide.[12] Fentanyl alone has more than 70 identified analogues, some of which are more potent than fentanyl (e.g., carfentanil, 100× more potent than fentanyl), and opioid derivatives constitute 30% of the ∼550 identified NPSs in 2020.[12] Drug-targeting vaccines and monoclonal antibodies (mAbs) offer viable and adaptable strategies against F/FA and NPSs.[13−15] While vaccines elicit polyclonal antibodies over time, mAbs are able to immediately and directly sequester targeted drugs providing emergency overdose reversal by a mechanism distinct from that of naloxone and can be easily combined with existing MAT. Due to the structural diversity of F/FA, development of immunotherapeutics applicable to specific clinical scenarios may require a combination of rationally designed haptens and antibody engineering to tailor mAb binding sites to structures of new and emerging compounds.

The goal of the current work is to elucidate the binding modes of mAbs against fentanyl and carfentanil. Previously, we identified a series of conjugate vaccines targeting F/FA and have reported their preclinical efficacy against drug-induced hypoxia, apnea, bradycardia, and antinociception in mice, rats, and mini pigs.[16−19] These lead antifentanyl vaccines were used to isolate several mAbs (e.g., HY6-F9 and HY11-7E1) specific for F/FA,[20,21] which were humanized to generate mAb suitable for clinical development. Despite these efforts, the affinity of previously described mAbs for carfentanil was limited. The present study reports a series of novel mAbs (HY17-2A2, HY17-4A5, HY18-5B1, and HY19-1H6) isolated from mice after immunization with a combination of vaccines against fentanyl and carfentanil and compares these novel mAbs to previously published mAbs for their *in vivo* efficacy against F/FA. This study uses X-ray crystallography to further explore the structures of three mAbs (HY11-7E1, HY11-6B2, HY18-5B1) bound to fentanyl or carfentanil, detailing similarities in binding modes that identified critical binding residues and enabled structure-informed site-directed mutagenesis (SDM) to improve their binding.

RESULTS

***In Vitro* Affinity of mAb Predicts *In Vivo* Efficacy against Fentanyl and Fentanyl Analogues.** The murine antifentanyl mAbs HY6-F9 and HY11-7E1 previously showed similar affinities for fentanyl (∼3 nM), while HY11-7E1 showed a 15-fold higher affinity for acetylfentanyl and 6-fold higher affinity for carfentanil than HY6-F9.[20] To illustrate the relationship between mAb affinity, drug potency, and mAb efficacy *in vivo* against fentanyl and these analogues, mice were passively immunized with 40 mg/kg murine HY6-F9 or HY11-7E1. Then, 24 h later, mice were challenged with fentanyl at 0.1 mg/kg or with an approximately equipotent dose of acetylfentanyl (1.0 mg/kg) or carfentanil (0.02 mg/kg). Notably, because the mAb dose was the same but the drug dose varied according to their relative potency, the molar mAb:drug dose ratios were approximately 1.8 for fentanyl, 0.17 for acetylfentanyl, and 10 for carfentanil. All three drugs induced antinociception and reduced heart rate and breath rate in saline-treated mice; only carfentanil reduced oxygen saturation below the predrug baseline (Figure S1). Both HY6-F9 and HY11-7E1 reduced the effects of fentanyl on the heart rate (Figure S1B) and significantly altered the distribution of fentanyl (Figure 1A). HY6-F9 also significantly reduced the effects of fentanyl on the breath rate (Figure S1C). HY11-7E1 significantly increased acetylfentanyl in serum, and both HY6-F9 and HY11-7E1 significantly reduced acetylfentanyl in the brain by approximately 50% (Figure 1B). Both mAbs reduced the effects of acetylfentanyl on the heart rate. Finally, HY11-7E1, but not HY6-F9, significantly increased carfentanil in serum and nonsignificantly reduced carfentanil in the brain ($p = 0.0966$) by about 45% (Figure 1C).

Active Immunization with Structurally Diverse Haptens Elicits mAbs with Affinity for Fentanyl and Carfentanil. To isolate mAbs with higher affinity for F/FA, such as carfentanil, mice were immunized with the carfentanil-

https://doi.org/10.1021/acsomega.4c06617
ACS Omega 2024, 9, 42506−42519

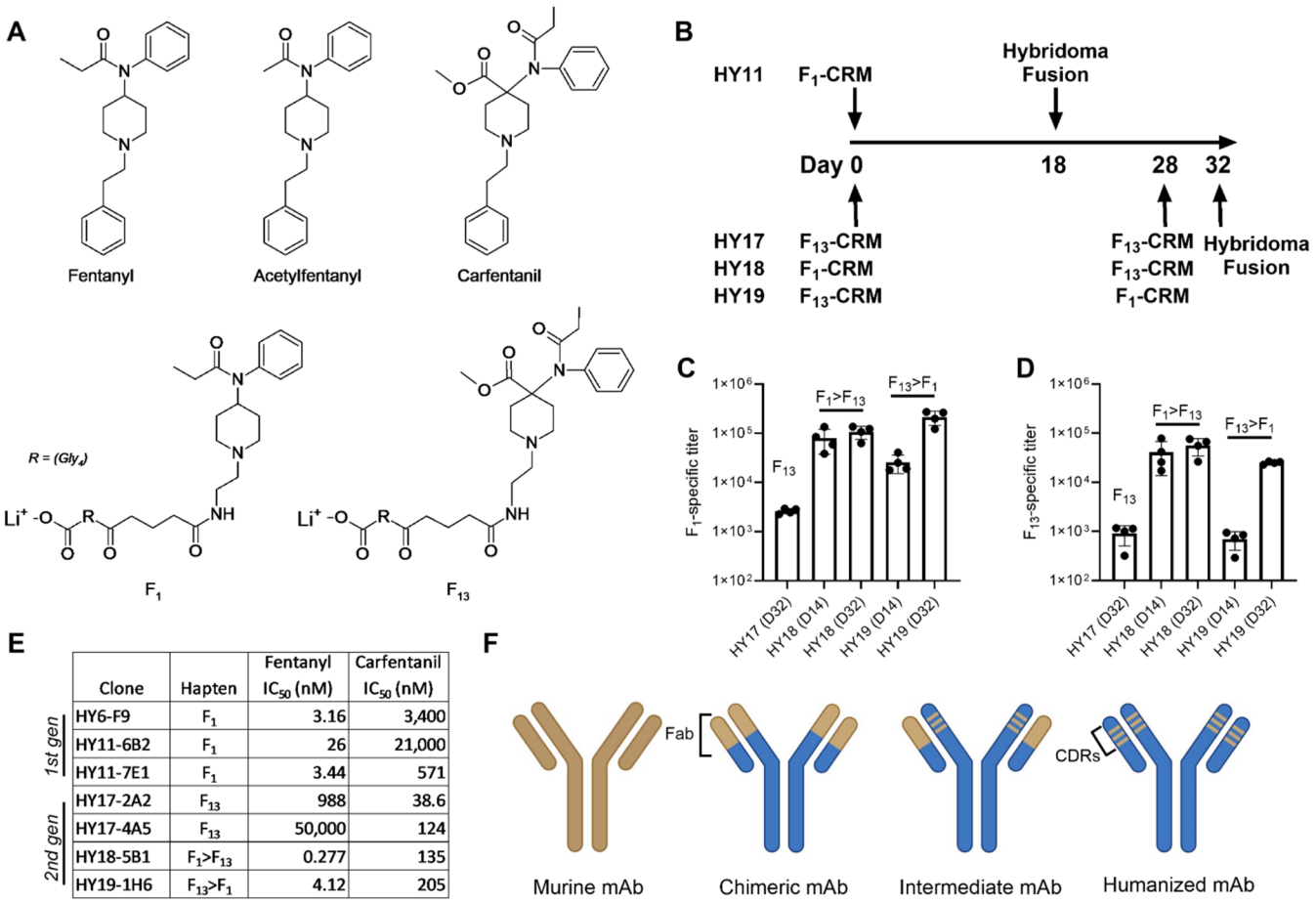

	Clone	Hapten	Fentanyl IC_{50} (nM)	Carfentanil IC_{50} (nM)
1st gen	HY6-F9	F_1	3.16	3,400
1st gen	HY11-6B2	F_1	26	21,000
1st gen	HY11-7E1	F_1	3.44	571
2nd gen	HY17-2A2	F_{13}	988	38.6
2nd gen	HY17-4A5	F_{13}	50,000	124
2nd gen	HY18-5B1	F_1>F_{13}	0.277	135
2nd gen	HY19-1H6	F_{13}>F_1	4.12	205

Figure 2. Isolation of novel mAbs using fentanyl- and carfentanil-based haptens. (A) Structures of F/FA, fentanyl-based hapten F_1, and carfentanil-based hapten F_{13}. (B) Immunization scheme for the isolation of novel mAbs. Mice were immunized with F_1-CRM or F_{13}-CRM as shown. (C) F_1-specific (fentanyl) ELISA titer in mouse sera after one (day 14) or two (day 32) immunizations with F_1-CRM or F_{13}-CRM. Labels above bars indicate the order of immunization. (D) F_{13}-specific (carfentanil) ELISA titer in mouse serum after one or two immunizations with F_1-CRM or F_{13}-CRM. (E) Relative affinity (IC_{50}) for murine mAbs against fentanyl or carfentanil was determined by competitive ELISA. Values for HY6-F9, HY11-6B2, and HY11-7E1 were previously published and are included here for comparison (www.tandfonline.com).[20] (F) Diagram of the mAb humanization scheme showing regions of murine residues in tan or human residues in blue.

based hapten F_{13}-CRM (Figure 2A), which was previously shown to elicit fentanyl- and carfentanil-specific polyclonal IgG in rats,[18] alone or in combination with F_1-CRM. Notably, both F_1 and F_{13} are conjugated in the same orientation, with the linker replacing the phenyl moiety, which presents the molecule's polar functional groups to the B-cell receptor (BCR) pocket.[15,22] To assess responses to different active immunization strategies, mice were vaccinated as follows: twice with F_{13}-CRM to generate HY17 mAbs, once with F_1-CRM followed by a boost with F_{13}-CRM to generate HY18 mAbs, or once with F_{13}-CRM followed by a boost with F_1-CRM to generate HY19 mAbs (Figure 2B). Murine immune sera were assessed by ELISA, and all mice showed detectable F_1-specific and F_{13}-specific titers (Figure 2C,D), although the increase in titer elicited by F_1-CRM was larger than that for F_{13}-CRM in both combinations. Hybridomas were generated from splenocytes, and four novel "second-generation" mAbs were isolated and tested for relative affinity for fentanyl and carfentanil by competitive ELISA (Figure 2E) compared to values for F_1-specific "first-generation" mAbs.[20] HY17-2A2 and HY17-4A5 showed the highest affinity for carfentanil and very low affinity for fentanyl, while HY18-5B1 and HY19-1H6 showed mid-level to low nanomolar affinity for both fentanyl and carfentanil.

Novel Chimeric mAbs Alter the Distribution of Fentanyl/Carfentanil Mixtures. The variable regions (VH and VL) of second-generation mAbs were sequenced and cloned into expression vectors containing the constant regions of human IgG_1 and IgK to produce chimeric (_Ch) mAbs (Figure 2F). We compared these chimeric second-generation mAbs to HY11-7E1_Ch. Mice were passively immunized with 40 mg/kg HY11-7E1_Ch or second-generation mAbs HY17-2A2_Ch, HY17-4A5_Ch, HY18-5B1_Ch, or HY19-1H6_Ch, and efficacy was evaluated against fentanyl, carfentanil, and their mixture. Mice were first challenged with 0.1 mg/kg fentanyl 24 h after passive immunization (day 1) and then challenged with 0.01 mg/kg carfentanil (day 2), and the effect of mAb on opioid-induced antinociception was assessed 30 min after each challenge (Figure S2). The chimeric mAbs HY11-7E1_Ch, HY18-5B1_Ch, and HY19-1H6_Ch reduced fentanyl-induced antinociception, but no mAbs showed a significant effect against carfentanil-induced antinociception at this dose. Finally, on day 3, mice were challenged with a mixture of 0.05 mg/kg fentanyl + 0.005 mg/kg carfentanil to determine mAbs' effects on target drug distribution (Figure 3).

https://doi.org/10.1021/acsomega.4c06617
ACS Omega 2024, 9, 42506−42519

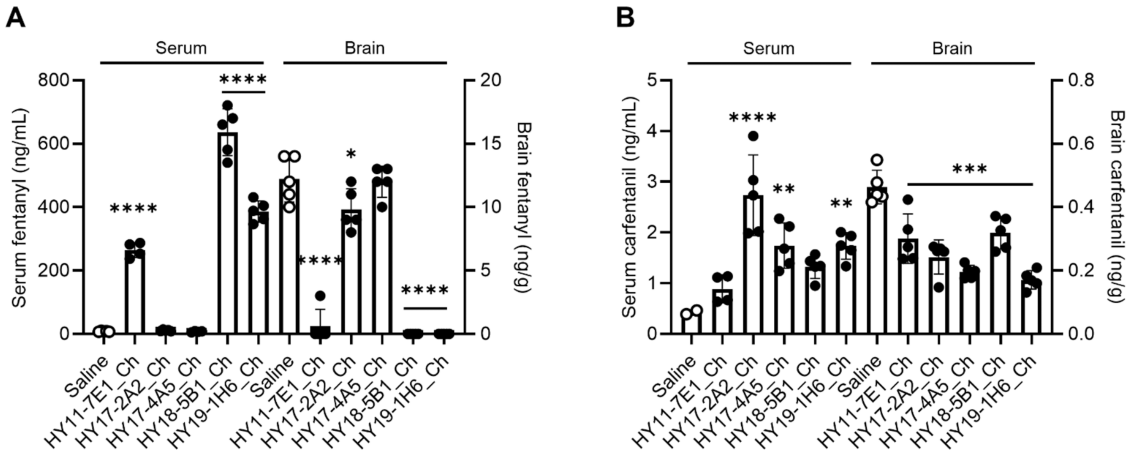

Figure 3. Efficacy of novel mAb against fentanyl and carfentanil. Mice (n = 5/group) were passively immunized with chimeric mAb, 40 mg/kg, s.c. and then challenged with a mixture of 0.05 mg/kg fentanyl and 0.005 mg/kg carfentanil on day 3. Concentrations of (A) fentanyl and (B) carfentanil in serum (left y-axis) and brain (right y-axis) were measured 30 min after drug administration. *p < 0.05, **p < 0.01, ***p < 0.001, ****p < 0.0001 compared to saline control.

Table 1. Affinity of HY18-5B1 Chimeric and Intermediate mAbs by BLI for F_1- and F_{11}-Biotin[a]

VH	VL	F_1-biotin K_D, M (mean ± error)	F_{11}-biotin K_D, M (mean ± error)
HY11-5B1 murine	HY11-5B1 murine	$<(1.0 \pm 7.74) \times 10^{-12}$	$<(1.0 \pm 76.3) \times 10^{-12}$
HY11-5B1 humanized	HY11-5B1 murine	$(5.02 \pm 1.04) \times 10^{-11}$	$(1.63 \pm 0.095) \times 10^{-8}$
HY11-5B1 murine	HY11-6B2 humanized	$<(1.0 \pm 14.1) \times 10^{-12}$	no binding

[a]F_1, fentanyl-derived hapten; F_{11}, carfentanil-derived hapten.

Consistent with the experiment in Figure 1, HY11-7E1_Ch significantly altered both the fentanyl distribution and the carfentanil distribution. All four second-generation mAbs significantly reduced carfentanil distribution to the brain, but HY17-2A2_Ch and HY17-4A5_Ch showed a negligible effect on fentanyl distribution, consistent with their low affinity for fentanyl *in vitro*.

Fentanyl and Carfentanil Binding Depends on Both CDRs and Framework Regions. Because HY18-5B1 showed the highest affinity for fentanyl and a higher carfentanil affinity than HY11-7E1, it was selected for further development including humanization. Compared to HY11-6B2 and HY11-7E1, HY18-5B1 had different heavy chain (HC) germline and CDR sequences, but the same light chain (LC) germline and nearly identical CDR sequences (Table S1). A sequential CDR grafting humanization strategy was used for HY18-5B1, in which HC and LC are humanized separately and first paired with the corresponding murine chain to mitigate the loss of binding that can occur during humanization (Figure 2F). For HY18-5B1, murine HC CDRs were grafted onto human germline IGHV1-8*03 (a human germline similar to murine IGHV14-3*02), and because of the high LC homology, the humanized LC (using human germline IGKV1-16*01) from HY11-6B2 was used. Pairing the humanized HC with chimeric LC containing murine VL resulted in a reduction of binding to both fentanyl and carfentanil, and pairing the HY18-5B1 chimeric HC with the humanized LC resulted in a total loss of carfentanil binding (Table 1). Because we previously observed some loss of binding during humanization of HY11-7E1_Hu (DE), using the same humanized LC,[20] we hypothesized that framework residues not included in the grafted CDR regions may be required for binding to the target ligands.

Structural Comparisons of the 7E1 mAb Family Illustrate Deep-Pocketed Cross-Reactive Binding. To identify critical residues in the murine and humanized mAbs, we performed X-ray crystallography on 6B2_Mu, 7E1_Mu, and 7E1_Hu (DE). These mAbs share the same LC germline gene and similar HC germline genes (Table S1), making structural comparisons of these mAbs an ideal target to interrogate features that are key to high-affinity binding. We determined the structures of four Fabs by X-ray crystallography in the presence or absence of a ligand: 6B2_Mu:fentanyl, 7E1_Mu:fentanyl, 7E1_Hu (DE):F_{11}, and 7E1_Hu (DE) Apo. We solved the structure of 6B2_Mu:fentanyl to a resolution of 2.3 Å (Figure 4A and Table 2), with eight Fabs in the unit cell, and found significant (~50%) tNCS during processing (Figure S3). We solved the 7E1_Mu:fentanyl complex structure to a resolution of 2.1 Å (Figure 4B and Table 2) and observed two Fabs in the unit cell, with no major deviations in binding mode or orientation between copies. The humanized mAb 7E1_Hu (DE) bound to biotinylated carfentanil hapten F_{11} (Figure 4A and Table 2) was solved to a resolution of 2.4 Å. Again, we noted two Fabs in the unit cells, with no major deviations between copies. The biotinylated F_{11} hapten is not well resolved beyond the apical nitrogen group (Figure 2A). We also solved the structure of 7E1_Hu (DE) to 2.2 Å in the absence of a ligand, with four Fabs in the unit cell.

The structural similarities among 6B2_Mu, 7E1_Mu, and 7E1_Hu (DE) are shown in Figure 4A–C. Structure alignments highlight these similarities: the root-mean-square deviation (RMSD) between 6B2_Mu and 7E1_Mu is 0.589 Å over the VH/VL region (198 Cα) (Figure 4D) and 0.688 Å over the VH/VL region (192 Cα) when comparing 7E1_Mu and 7E1_Hu (DE) (Figure 4E). Kabat[23] antibody numbering is used throughout our results and discussion of these structures. All three antibodies show that the ligand is oriented vertically (Figure 4A), with residues $Glu95_{HC}$ and $Tyr55_{LC}$ making contact with the piperidine ring nitrogen. As we[22] and

https://doi.org/10.1021/acsomega.4c06617
ACS Omega 2024, 9, 42506−42519

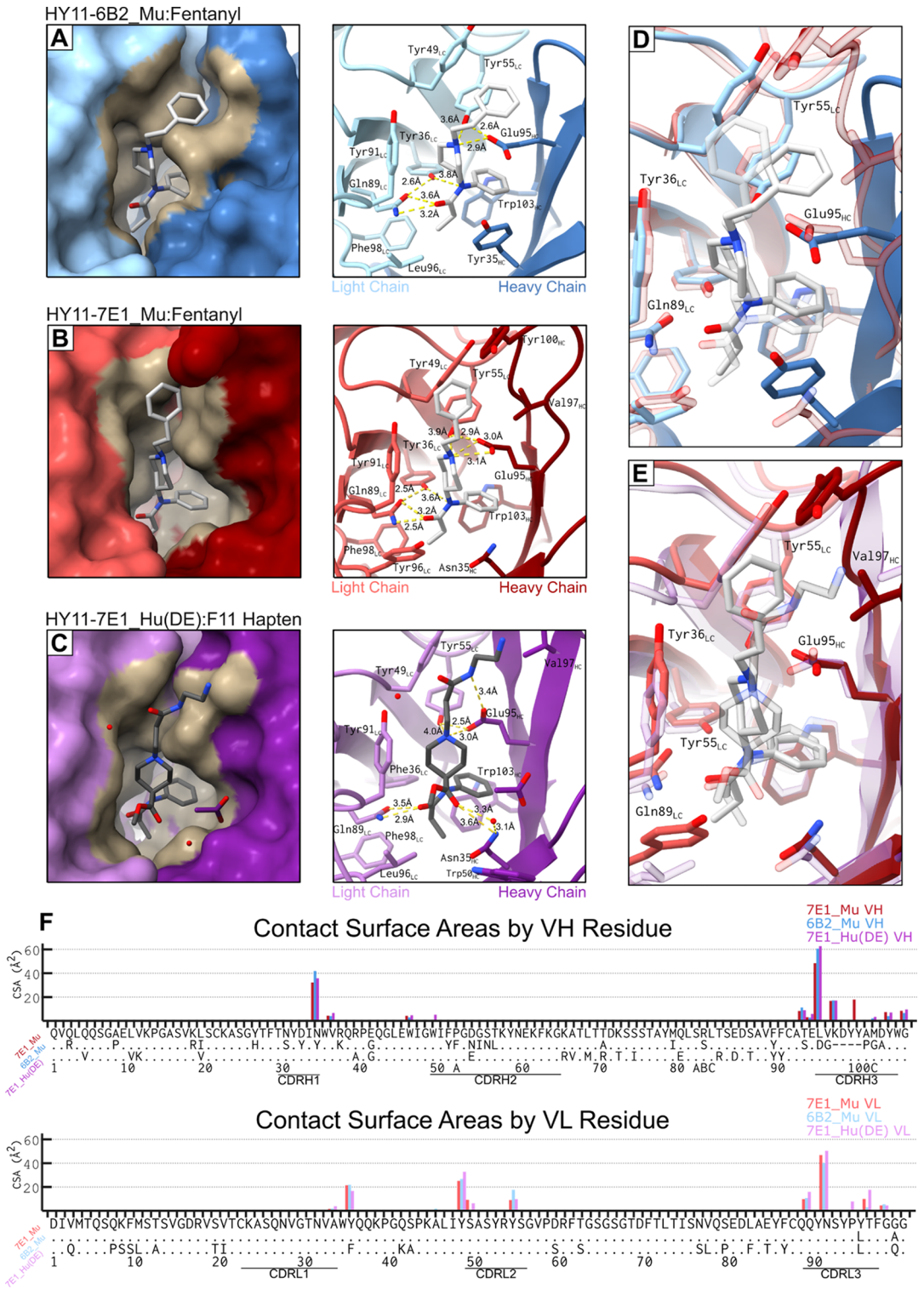

Figure 4. Crystal structures and sequence comparisons of 6B2_Mu:fentanyl, 7E1_Mu:fentanyl, and 7E1_Hu (DE):F_{11}. (A) Left: Surface representation of the binding pocket of 6B2_Mu Fab with fentanyl in gray. Surface within 4 Å of fentanyl is colored in tan. Right: Stick representations of the same view. Potential polar bonds are shown in yellow. (B) Left: Surface representation of 7E1_Mu Fab with fentanyl in gray shown in the same manner as panel (A). Right: Stick representation of the same view. Bonds and orientations are the same as described in panel (A). (C) Left: Surface representation of 7E1_Hu (DE) Fab with F_{11} hapten is shown in the same manner as panel (A). Red dots indicate the positions of water molecules in the structure. Right: Stick representation of the same view. Bonds and orientations are the same as described in panel (A). (D) Structural overlay of 6B2_Mu Fab and 7E1_Mu Fab, with 7E1_Mu Fab shown in transparency. The orientation is the same as panels (A) and (B), and the view is zoomed in. (E) Structural overlay of 7E1_Mu Fab and 7E1_Hu (DE) Fab, with 7E1_Hu (DE) shown in transparency. The orientation is the same as in panels (B) and (C), and the view is zoomed in. (F) Contact surface area (CSA) plot of the ligand when bound to 6B2_Mu, 7E1_Mu, or 7E1_Hu (DE). Sequence alignments of the VH and VL regions of each mAb are shown. Dots show conserved residues with 7E1_Mu as the template. Dashes indicate gaps. Numbering and CDRs are true to 7E1_Mu.

https://doi.org/10.1021/acsomega.4c06617
ACS Omega 2024, 9, 42506−42519

Table 2. Data Collection and Refinement Statistics for Crystal Structures

	HY11-6B2_Mu:fentanyl	HY11-7E1_Mu:fentanyl	HY11-7E1_Hu_DE:F11	HY11-7E1_Hu_DE Apo	HY18-5B1_Mu:fentanyl	HY18-5B1_Mu Apo
			Data Collection			
space group	P1	$P4_1$	I121	$P12_11$	$P3_1$	C121
cell dimensions						
a, *b*, *c* (Å)	69.78, 98.24, 159.72	60.52, 60.52, 259.86	46.16, 154.89, 159.76	72.58, 151.10, 104.60	114.71, 114.71, 90.86	94.33, 61.32, 76.58
α, *β*, *γ* (deg)	77.73, 85.32. 77.95	90, 90, 90	90, 90.63, 90	90, 91.14, 90	90 90 120	90 103.88 90
resolution (Å)	49.37−2.20 (2.24−2.20)	50.0−1.98 (2.01−1.98)	49.13−2.17 (2.23−2.17)	50.00−2.20 (2.24−2.20)	50.00−2.40 (2.44−2.40)	50.00−2.04 (2.08−2.04)
R_{merge}[a]	0.135 (1.201)	0.84 (3.505)	0.123 (2.043)	0.132 (0.876)	0.243 (4.721)	0.116 (0.429)
$\langle I/\sigma(I)\rangle$	4.4 (0.6)	4.5 (0.5)	6.5 (0.6)	7.4 (0.7)	4.8 (0.0)	15.4 (3.0)
$CC_{1/2}$	0.985 (0.218)	0.967 (0.029)	0.996 (0.646)	0.978 (0.417)	0.884 (0)	0.974 (0.710)
completeness	96.9 (92.7)	98.3 (87.0)	98.98 (98.6)	95.7 (76.1)	98.7 (94.2)	98.5 (97.4)
redundancy	1.8 (1.6)	5.5 (2.1)	3.3 (2.7)	2.5 (1.9)	3.2 (1.0)	1.7 (1.7)
			Refinement			
resolution (Å)	50.00−2.20 (2.279−2.2)	50.00−2.10 (2.175−2.1)	49.13−2.40 (2.486−2.40)	50.00−2.20 (2.279−2.20)	41.32−3.30 (3.42−3.30)	45.79−2.04 (2.11−2.04)
no. of unique reflections	198 836 (19 048)	53 890 (5348)	43 366 (4356)	109 558 (10 271)	19 876 (1916)	26 775 (2622)
R_{work}[b]/R_{free}[c]	24.2/27.3 (35.2/36.2)	22.1/25.3 (32.1/37.0)	24.0/26.6 (32.1/35.8)	20.8/23.7 (35.4/39.6)	30.0/37.8 (39.4/40.1)	24.4/26.8 (27.4/30.2)
no. atoms	27 105	7036	6591	13 485	9181	3433
protein	25 864	6608	6278	13 028	9131	3242
water	876	228	247	393	0	179
ligand	365	200	66	64	50	12
B-factors (Å^2)	41.47	46.64	63.44	55.15	116.72	41.42
protein	41.43	46.50	64.09	55.19	116.73	41.51
water	41.00	43.46	48.85	52.00	0	40.08
ligand	45.05	55.01	56.32	65.84	115.63	36.45
RMS bond length (Å)	0.007	0.005	0.087	0.003	0.003	0.002
RMS bond angle (deg)	1.02	0.95	0.67	0.62	0.57	0.52
			Ramachandran plot statistics[d]			
residues	3392	868	834	1706	1299	433
most favored region	96.73	96.97	96.67	97.32	89.20	97.44
allowed region	3.15	2.80	3.08	2.62	9.95	2.33
disallowed region	0.12	0.23	0.25	0.06	0.85	0.23
clash score	1.32	6.03	3.65	7.52	9.83	6.61
PDB ID	9AXN	9AXO	9AXP	9AXQ	9AXR	9AXS

[a] $R_{merge} = [\sum_h\sum_i|I_h - I_{hi}|/\sum_h\sum_i I_{hi}]$, where I_h is the mean of I_{hi} observations of reflection *h*. Numbers in parentheses represent the highest resolution shell. [b] $R_{factor} = \sum||F_{obs}| - |F_{calc}||/\sum|F_{obs}| \times 100$ for 95% of recorded data. [c] $R_{free} = \sum||F_{obs}| - |F_{calc}||/\sum|F_{obs}| \times 100$ for 5% data. [d] Determined using MolProbity (10.1002/pro.3330).

others[24−26] have observed, there is a high probability that both fentanyl and carfentanil are protonated at this piperidine nitrogen. This positively charged quaternary amine is coordinated by $Glu95_{HC}$, forming a salt bridge, while $Tyr55_{LC}$ likely forms an additional hydrogen bond with $Glu95_{HC}$. The *N*-phenyl ring is sequestered underneath the extended $Glu95_{HC}$, protruding deeper into the pocket. On the opposite side of fentanyl from $Glu95_{HC}$, $Tyr91_{LC}$ forms van der Waals contacts with the bulk of the piperidine ring, creating a narrow point in the pocket and facilitating $Glu95_{HC}$ coordination. All three structures also share $Gln89_{LC}$, which binds the fentanyl ketone opposite that of $Glu95_{HC}$ and under $Tyr91_{LC}$. 7E1_Mu and 6B2_Mu contain $Tyr36_{LC}$, which is an additional residue in the $Gln89_{LC}$/ketone hydrogen bond network; 7E1_Hu (DE) lacks this residue and instead has $Phe36_{LC}$, a germline residue from the human IGKV1-16*01 gene. In addition, there are small variations in the binding angle of $Tyr55_{LC}$ and $Glu95_{HC}$ (Figure 4D,E) to accommodate variations in the ligand position, especially for F_{11}. In all three structures, $Glu95_{HC}$ maintains an ∼3 Å contact with the piperidine nitrogen and the nitrogen−hydrogen−oxygen angle is within 140−160°. Together, these features suggest salt-bridge coordination between a glutamic acid and an amine.[27] In the 7E1_Hu (DE):F_{11} structure (Figure 4C, panel 2), the F_{11} hapten contains a secondary amine not present in carfentanil (Figure 2A). This amine coordinates $Glu95_{HC}$ when F_{11} binds and may explain the difference in $Glu95_{HC}$ orientation between structures. Near the solvent-exposed side, 7E1_Hu (DE) contains an additional hydrogen-bonding motif at $Asn35_{HC}$ that coordinates with the ester group of carfentanil. There is some sequence variation on this solvent-exposed side at LC residue 96 (Tyr versus Leu) and HC residue 35 (Tyr versus Asn) (Figure 4D,E). The most significant variation between these mAbs is the CDRH3 length. The CDRH3 of 6B2_Mu is shorter than those of 7E1_Mu and 7E1_Hu (DE) by four residues (Figure 4F). Structurally, there are minimal differences in the contact surface area (CSA) between the Fab and its bound drug despite this difference in CDRH3 (Figure

https://doi.org/10.1021/acsomega.4c06617
ACS Omega 2024, 9, 42506−42519

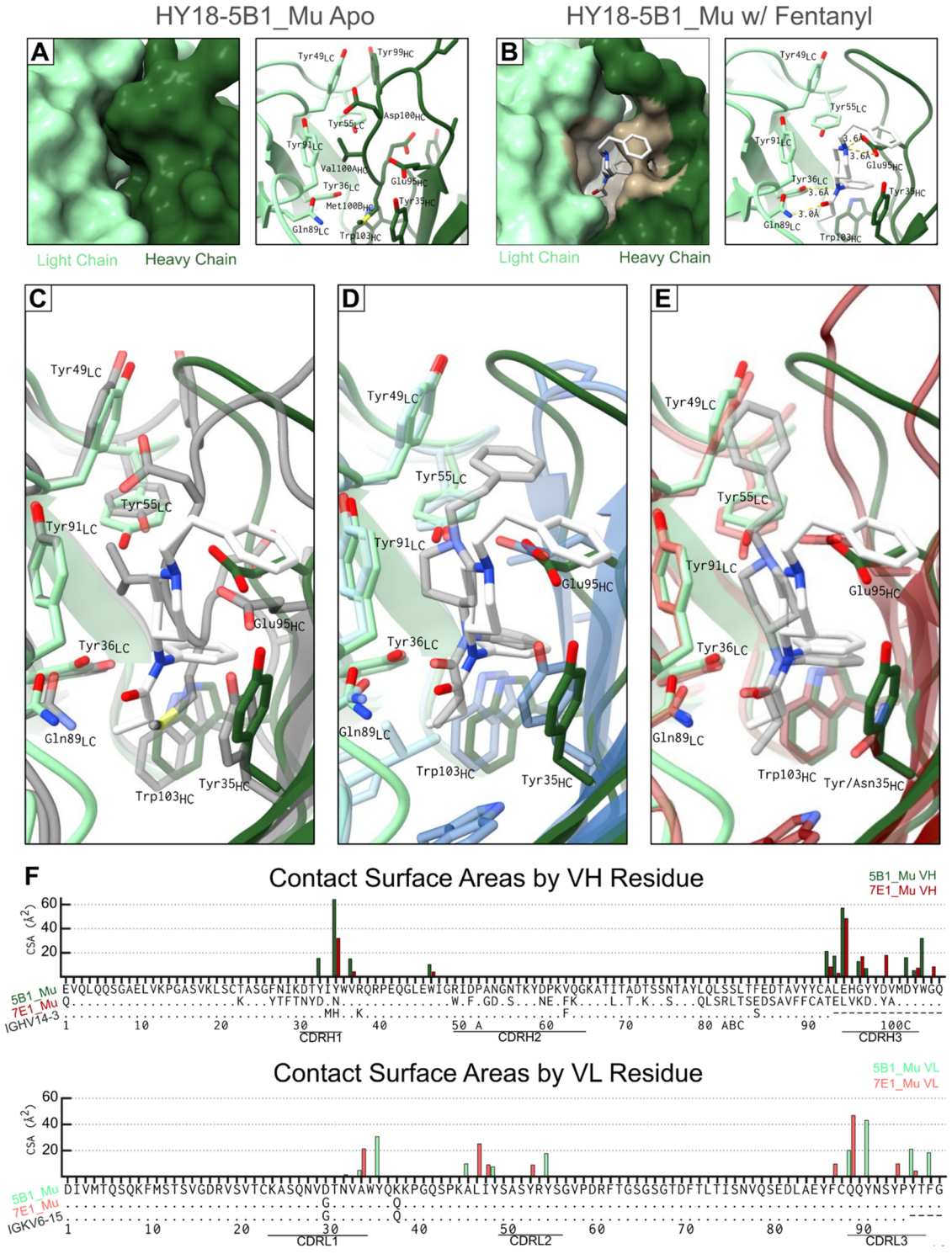

Figure 5. Crystal structures of 5B1_Mu Apo and 5B1_Mu:fentanyl. (A) Left: Surface representation of the 5B1_Mu Fab apo showing the binding pocket of 5B1_Mu. Right: Stick representation of the same view. (B) Left: Surface representation of 5B1_Mu Fab complexed with fentanyl is shown in the same manner as panel (A). Surfaces within 4 Å of fentanyl are colored in tan. Right: Stick representation of the same view. The orientation is equivalent to that in panel (A). Fentanyl is shown in light gray. Bonds are shown in yellow with distances listed. (C) Structural overlay of 5B1_Mu Apo versus 5B1_Mu:fentanyl. The orientation is the same as in panels (A) and (B). Distances and bonds are omitted for clarity. (D) Structural overlay of 5B1_Mu Fab bound to fentanyl (green) and 6B2_Mu Fab bound to fentanyl (blue transparency). The orientation is the same as in panel (B). Distances are omitted for clarity. (E) Structural overlay of 5B1_Mu Fab bound to fentanyl (green) and 7E1_Mu Fab bound to fentanyl (red transparency). The orientation is the same as in panel (B). Distances are omitted for clarity. (F) CSA with a plot of the ligand when bound to 5B1_Mu or 7E1_Mu, with sequence alignments of the VH and VL regions of 5B1_Mu, compared to 7E1_Mu and the murine germline IGKV6-15. Dots show conserved residues with 5B1_Mu as a template. Dashes indicate gaps. Numbering and CDRs are true to 5B1_Mu.

https://doi.org/10.1021/acsomega.4c06617
ACS Omega 2024, 9, 42506−42519

Table 3. Affinity of mAb Mutants by BLI for F_1-Biotin and F_{11}-Biotin

parent mAb ID	VH	VL	F_1-biotin K_D, M (mean ± error)	F_{11}-biotin K_D, M (mean ± error)
HY11-6B2_Ch	6B2 murine	6B2 murine	$<(1.0 \pm 12.9) \times 10^{-12}$	no binding
HY11-6B2_Ch	6B2 murine Glu95Ala	6B2 murine	$(7.12 \pm 0.129) \times 10^{-9}$	n/a
HY11-6B2_Ch	6B2 murine Glu95Gln	6B2 murine	$(3.63 \pm 0.0575) \times 10^{-9}$	n/a
HY11-6B2_Ch	6B2 murine	6B2 murine Gln89Ala	$<(1.0 \pm 0.215) \times 10^{-10}$	n/a
HY11-6B2_Ch	6B2 murine Glu95Ala	6B2 murine Gln89Ala	no binding	n/a
HY11-6B2_Ch	6B2 murine Glu95Gln	6B2 murine Gln89Ala	no binding	n/a
HY11-6B2_Ch	6B2 murine Trp50Arg	6B2 murine	$(2.20 \pm 0.094) \times 10^{-10}$	no binding
HY11-6B2_Ch	6B2 murine Trp50Gly	6B2 murine	$(1.68 \pm 0.012) \times 10^{-9}$	no binding
HY18-5B1_Int	5B1 murine	6B2 humanized Leu96Tyr	$<(1.0 \pm 16.5) \times 10^{-12}$	no binding
HY18-5B1_Int	5B1 humanized Trp50Arg	5B1 murine	no binding	no binding
HY18-5B1_Int	5B1 humanized Trp50Gly	5B1 murine	$(7.72 \pm 0.105) \times 10^{-10}$	no binding
HY18-5B1_Int	5B1 murine	6B2 humanized Phe36Tyr	$<(1.0 \pm 1.0) \times 10^{-12}$	$(8.70 \pm 0.173) \times 10^{-10}$
HY18-5B1_Hu	5B1 humanized	6B2 humanized Phe36Tyr	$(3.25 \pm 0.036) \times 10^{-10}$	$(5.66 \pm 0.030) \times 10^{-9}$
HY11-7E1_Hu (DE)	7E1 humanized	6B2 humanized	$(5.60 \pm 1.15) \times 10^{-11}$	$(1.31 \pm 0.038) \times 10^{-9}$
HY11-7E1_Hu (DE)	7E1 humanized	6B2 humanized Phe36Tyr	$<(1.0 \pm 1.0) \times 10^{-12}$	$(1.49 \pm 1.49) \times 10^{-12}$

Table 4. Affinity of HY6-F9_Hu (NQ) and HY11-7E1_Hu (DE) Fab Mutants by BLI for F_1-Biotin and F_{11}-Biotin

parent mAb ID	hapten	mutation	K_D, M (mean ± error)	K_{on}	K_{off}	full R^2
HY11-7E1_Hu (DE)	F_1-biotin	WT	$(7.91 \pm 0.300) \times 10^{-9}$	6.44×10^{05}	5.10×10^{-03}	0.931
HY11-7E1_Hu (DE)	F_1-biotin	$Gln89His_{LC}$	$(6.32 \pm 0.185) \times 10^{-9}$	5.45×10^{05}	3.44×10^{-03}	0.9468
HY11-7E1_Hu (DE)	F_{11}-biotin	WT	$(1.334 \pm 0.0752) \times 10^{-7}$	4.25×10^{06}	5.67×10^{-02}	0.9965
HY11-7E1_Hu (DE)	F_{11}-biotin	$Gln89His_{LC}$	$(5.478 \pm 3.03) \times 10^{-7}$	2.11×10^{05}	1.16×10^{-01}	0.9816
HY6-F9_Hu (NQ)	F_1-biotin	WT	$(1.42 \pm 0.0412) \times 10^{-8}$	3.35×10^{05}	4.75×10^{-03}	0.9666
HY6-F9_Hu (NQ)	F_1-biotin	$Asp98Asn_{HC}/Asn99Asp_{HC}$	$(1.26 \pm 0.0318) \times 10^{-8}$	3.71×10^{05}	4.69×10^{-03}	0.9714

4F). In 6B2_Mu, the shorter CDRH3 is locked in a β-sheet adjacent to the ligand, while the 7E1_Mu CDRH3 is in closer proximity to the ligand (Figure 4D). This rigid CDRH3 may contribute to 6B2_Mu reduced binding to carfentanil, lacking the flexibility to accommodate a larger ligand.

In the 7E1_Hu (DE) Apo structure, the pocket is solvent-filled with water coordinated at unbound polar residues. Residue positions are unchanged between the Apo and bound forms, and ligand ingress into the pocket is unlikely to occur without rearrangement (Figure S4A). While there is some shifting of the CDRH3 following binding, the overall structure of 7E1_Hu (DE) bound to carfentanil remains similar to the Apo form (with an RMSD of 0.486 Å over the VH/VL region containing 223 Cα) (Figure S4B). CDRH3 is a β-sheet in the Apo conformation (Figure S4A). This sheet becomes disrupted following fentanyl binding, moving away from the ligand slightly, while the CDRH3 apex, $Tyr100_{HC}$, curves over the ligand, helping to lock it into place (Figure S4B). This "capping" of the ligand is not seen in the 7E1_Hu (DE):F_{11} structure (Figure S4C), where the CDRH3 moves away from the ligand due to the F_{11} linker clashing with the normal position of the CDRH3; this is also visible in Figure 4E, where the linker is shown nearly touching $Val97_{HC}$. When carfentanil is bound, modeled *in silico* (Figure S4D), the lack of this linker may allow for a closer association between carfentanil and the CDRH3. Overall, these structures illustrate an open-and-close binding mechanism within the HY11-7E1 mAb family for F/FA ligands.

HY18-5B1 Displays Preferential Affinity for Carfentanil with a More Flexible CDRH3. To investigate the differences between the HY11 mAbs and HY18-5B1, we solved the structure of 5B1_Mu Apo at 2.1 Å resolution and the 5B1_Mu:fentanyl complex at 3.3 Å resolution. The 5B1_Mu:-fentanyl complex has three Fabs within the unit cell of a merohedral twinned crystal, with one Fab displaying density for fentanyl in the pocket. The 5B1_Mu pocket is distinct from that of 7E1 mAbs in the apo conformation. Rather than a structured, solvent-filled pocket, the CDRH3 moves to fill the pocket space and coordinate with the LC (Figure 5A). Upon ligand coordination, the distal region of CDRH3 (residues $100C_{HC}$ through 103_{HC}) becomes structured, forming an antiparallel β-sheet (Figure 5B,C) and highlighting the conformational change that 5B1 undergoes during ligand binding. Greater flexibility in the CDRH3 may allow 5B1_Mu to accommodate larger functional groups on the ligand, such as carfentanil. This increased flexibility also complicated crystallization, as 5B1_Mu:fentanyl was more resistant to well-ordered crystallization than ligand-bound 7E1 family mAbs.

The conformation of fentanyl in the pocket also differs between these mAbs. When 7E1_Mu binds to fentanyl, the fentanyl adopts only the "L" conformation (Figure 4B), while it adopts a "C" conformation when bound to 5B1_Mu (Figure 5B,E). The structure of 6B2_Mu bound to fentanyl shows a mix of "L" and "C" conformations of the fentanyl molecule (Figure 4A,D). These differences can be explained by 6B2_Mu having a CDRH3 that is shorter by five residues, as well as lacking residues that clash with the "C" conformation. $Val97_{HC}$ is present in all 7E1 structures and would clash with fentanyl in the "C" conformation (Figure 4D). 5B1_Ch lacks $Val97_{HC}$, instead having $Gly97_{HC}$ in its CDRH3. When 5B1_Mu is bound to fentanyl, the "C" conformation appears to be favored, as the CDRH3 arranges itself at the top of the pocket, trapping the ligand. Once bound, multiple key residues ($Glu95_{HC}$, $Tyr36_{LC}$, $Tyr55_{LC}$, $Gln89_{LC}$, and $Tyr91_{LC}$) adopt a conformation similar to the ones in 7E1-like mAb structures.

Mutational Studies Confirm Residues Contributing to Binding. We performed mutational studies on 6B2_Mu mAb to test the roles of $Glu95_{HC}$ and $Gln89_{LC}$ residues in ligand

https://doi.org/10.1021/acsomega.4c06617
ACS Omega 2024, 9, 42506−42519

coordination and uncover potential mutations to improve F/FA binding in humanized mAbs (Table 3). As $Glu95_{HC}$ displays a salt-bridge potential, we sought to examine whether this specific feature is required for drug binding. Mutation of the $Glu95_{HC}$ residue to either Gln or Ala resulted in a lower affinity to F_1-biotin (Table 3) and an increase of several orders of magnitude in K_D resulting from a higher K_{off} of the mutants (Figure S5A). Mutation of $Gln89_{LC}$ to Ala also resulted in a lower affinity to F_1-biotin (a smaller increase in K_D), suggesting differences in the strength of these contacts. Furthermore, pairing $Gln89Ala_{LC}$ with either $Glu95_{HC}$ mutations ablated binding to the F_1-biotin hapten (Table 3), highlighting the impact of these two specific residues and their coordination networks (Figure 3A−C). This also suggests that van der Waals forces in this pocket are not sufficient to retain fentanyl in the absence of strong electrostatic connections.

We then attempted to enhance the binding of 7E1_Hu (DE) Fab by introducing a charged residue, histidine, in place of $Gln89_{LC}$ (Table 4). This experiment tested the hypothesis that using Fabs for BLI would be more sensitive to small changes in K_D and remove avidity effects versus using full-length mAb. The resulting mutated Fab, 7E1_Hu (DE) $Gln89His_{LC}$, maintained the same binding to fentanyl (F_1-hapten) (Table 4); however, reduced binding to carfentanil (F_{11}-hapten) by fivefold was observed, likely due to the increased size of histidine. In addition, the fentanyl-specific mAb HY6-F9_Hu[22,28] has a residue, $Asn99_{HC}$, with a structurally similar role to $Glu95_{HC}$ in 7E1 mAbs. To assess whether a similar residue with a stronger charge can improve electrostatic association, we made the mutation $Asp98Asn_{HC}$/$Asn99Asp_{HC}$ in HY6-F9_Hu Fab (Table 4). HY6-F9_Hu $Asp98Asn_{HC}$/$Asn99Asp_{HC}$ Fab bound to fentanyl by BLI (F_1 hapten) in a manner similar to its WT counterpart. While electrostatic complement appears to be essential to maintain ligand binding, increasing the potential electrostatic charge is not an effective method for improving the affinity of these mAbs.

We observed that both 7E1 and 5B1 lost binding when paired with the 6B2 humanized LC; in the LC, HY11-6B2_Mu and HY11-7E1_Mu show only three differences at the amino acid level (Figure 4F; 6B2 contains Leu_{96}, Ala_{100}, and Leu_{106}, while 7E1 contains Tyr_{96}, Gly_{100}, and Ile_{106}), and HY11-5B1_Mu is nearly identical to 7E1 with two amino acid differences from both HY11 mAbs (Figure 5F; 6B2 and 7E1 contain Gly_{30} and Gln_{38}, while 5B1 contains Asp_{30} and Lys_{38}); however, only Tyr_{96} is in a CDR (Table S1). Because $Tyr96_{LC}$ in 5B1_Mu appeared to have some contact with the ligand (Figure 5F), we tested 5B1_Mu HC with 6B2 humanized LC with $Leu_{96}Tyr$; however, binding was similar to that of humanized LC with Leu_{96}, indicating that this residue is not likely critical for binding.

Additionally, 6B2_Mu, 7E1_Mu, and 7E1_Hu (DE) share $Trp50_{HC}$, as does 5B1_Hu, whereas 5B1_Mu has an arginine at this position ($Arg50_{HC}$), and they showed the highest affinity for carfentanil. Hence, we engineered both 6B2_Ch and 5B1_Ch with $Trp50Gly_{HC}$ or $Trp50Arg_{HC}$. We expected these mutations to be able to better accommodate or coordinate the ester group of carfentanil that is not present in fentanyl since Gly is smaller than Trp and Arg is more flexible than Trp. Surprisingly, however, these mutations decreased the affinity of both mAbs to fentanyl and ablated binding of 5B1 to carfentanil (Table 3).

Structure-Guided Reversion of Murine Germline Residue Tyr36 Improves Cross-Reactive Binding in Humanized mAbs. Comparing the structure of 7E1_Hu (DE) bound to the carfentanil hapten F_{11} with that of 7E1_Mu bound to fentanyl (Figure 4E) shows that humanization had a minimal impact on the overall pocket structure. The humanized 7E1_Hu (DE) mAb showed almost no differences from 7E1_Mu in ligand CSA across the HC; in the LC, residues 36 and 96 showed changes in residue identity, although they did not change in ligand CSA (Figure 4F). Further analysis showed that $Phe36_{LC}$ in the 7E1_Hu (DE) structure lacked hydrogen bonding to the central amide nitrogen, whereas in 6B2_Mu and 7E1_Mu, $Tyr36_{LC}$ could form hydrogen bonds with both the central amide nitrogen and $Gln89_{LC}$ (Figure 4A−C, panel 2). Residue 36 is a framework (IGKV1-16*01) residue and was not included during CDR grafting to the human germline. To test the contribution of Tyr36 to binding, we tested the mutation $Phe36Tyr_{LC}$ in 7E1_Hu (DE), which improved fentanyl binding to <0.001 nM (a ∼56-fold increase) and improved carfentanil binding to 0.001 nM (a ∼881-fold increase) by BLI (Table 3). Interestingly, this difference was driven by a decrease in the BLI K_{off} (Figure S5), suggesting that $Tyr36_{LC}$ is important for retaining the bound ligand in the mAb pocket. Finally, to confirm that binding was improved against free drug and the F_1 and F_{11} haptens, we tested the relative affinity for fentanyl and carfentanil with competitive binding ELISA, comparing fully murine 7E1, 7E1_Ch, and 7E1_Hu (DE) against the mutant. Consistent with the BLI result, competitive ELISA using free drug showed an ∼3-fold increase in fentanyl binding and an ∼10-fold increase in carfentanil binding over 7E1_Hu (DE) (Table 5).

Table 5. Affinity of HY11-7E1 Mutants by Competitive ELISA for Fentanyl and Carfentanil

mAb ID	VH	VL	fentanyl IC_{50}, nM	carfentanil IC_{50}, nM
HY11-7E1_Mu	7E1 murine	7E1 murine	0.41	86.91
HY11-7E1_Ch	7E1 murine	6B2 murine	0.96	65.34
HY11-7E1_Hu (DE)	7E1 humanized	6B2 humanized	30.97	367.00
HY11-7E1_Hu (DE) F36Y	7E1 humanized	6B2 humanized Phe36Tyr	8.94	35.47

HY18-5B1 also lost carfentanil binding when paired with the 6B2 humanized LC, which contains $Phe36_{LC}$, while maintaining fentanyl binding (Table 1). As with HY11-7E1, the $Tyr36_{LC}$ mutation restored carfentanil binding when paired with both the 5B1 murine VH and the 5B1 humanized VH, but the affinity was not equivalent to that of HY18-5B1_Ch containing the fully murine Fab region (Table 1). Notably, 5B1 also showed a decrease in binding to both fentanyl and carfentanil when the murine LC was paired with the humanized HC. This suggests that there is a distinct issue with the humanized HC that results in decreased binding, regardless of $Tyr36_{LC}$. Further crystallographic data, such as the structure of 5B1 in complex with carfentanil, or of the 5B1 humanized LC and HC, are needed to determine which features are contributing to decreased drug affinity.

https://doi.org/10.1021/acsomega.4c06617
ACS Omega 2024, 9, 42506−42519

DISCUSSION

Translation of drug-specific mAbs is needed to address the existing fentanyl crisis and emerging illicit NPSs that are incompatible with existing interventions. To this end, this study reports antibody generation, humanization, and structure-based engineering to identify and optimize mAbs with an affinity for fentanyl and carfentanil. While development platforms for mAb identification have proliferated,[15] as have mAb modifications[24] or the use of adjuvants[19] for translational vaccines, there is still limited information on binding-site optimization. While some mAbs are highly specific for certain drugs,[15,22] others are "all-rounder" mAbs, which can bind many derivatives.[24,29] When considering the potency of carfentanil and the unknown characteristics of future NPSs, "all-rounder" mAbs may not have the same *in vivo* efficacy as highly specific binders. We must consider that, at least for opioids, mAbs are indirectly competing with the MOR, which has a 0.024 nM affinity for carfentanil.[30] Broadly cross-reactive mAbs also carry the risk of off-target binding to critical medications, including MOR ligands such as naloxone or buprenorphine.

The therapeutic potential of mAb to prevent[15,31,32] or even reverse[28,33] the effects of fentanyl has been well established in rodents and other animal models. A few studies have directly examined the ability of F/FA-targeting mAbs to prevent carfentanil effects *in vivo*.[33,34] The binding affinity of a mAb for a small-molecule target is a generally accepted predictor of efficacy, which is illustrated here by the effects of mAbs with different affinities on the serum concentrations of F/FA in mice. It is possible that the minimum affinity required to significantly alter the distribution of the target drug further depends on drug dose and potency, as well as pharmacokinetic properties such as distribution and metabolism. In the case of fentanyl, where most mAbs showed affinity <50 nM, the majority of the drug is redirected from the brain and other tissues to the blood, resulting in a high serum fentanyl concentration. Similar high serum concentrations were seen for acetylfentanyl. On the other hand, the serum carfentanil concentrations we observed were below 5 ng/mL (=12 nM), despite the mAb dose being in tenfold molar excess of the carfentanil dose in these experiments, with brain levels being reduced by half compared to controls. Therefore, we predicted that a carfentanil-targeting mAb would need to achieve an affinity <1 nM, or potentially lower, to prevent carfentanil distribution. However, further experiments are required to determine the ideal properties and dosing of mAbs targeting F/FA and to more thoroughly characterize the effects of these mAb on carfentanil-induced respiratory depression and antinociception and to test postexposure reversal of F/FA.

This study tested a combination of fentanyl-specific (F_1) and carfentanil-specific (F_{13}) vaccines as a strategy to generate hybridomas with an affinity for one or both drugs. While previous work found that this vaccine combination elicited a polyclonal antibody response against both drugs in rats, analysis of polyclonal antibodies could not distinguish between a mixed response of F_1-specific and F_{13}-specific antibodies versus a pool of cross-reactive antibodies. Here, we found that sequential immunizations with F_1 and F_{13} led to isolation of cross-reactive mAbs, while immunization with F_{13} alone generated mAbs with a low fentanyl affinity. This suggests that to facilitate targeted accommodation of multiple functional groups across F/FA, further sequential vaccinations with fentanyl-derivative haptens may allow greater binding diversity following the priming immunization.

The accommodation of additional functional groups present in F/FA is centered around strong amine coordination, a consistent key feature of opioid-binding mAbs.[14,15,22,24] Here, two amine coordinating sites are present: the amine-binding $Glu95_{HC}$ site, which forms a salt bridge, and the $Gln89_{LC}$ site, which networks with $Tyr36_{LC}$ in 6B2_Mu and 7E1_Mu but only involves $Gln89_{LC}$ in 7E1_Hu (DE) (Figure 4A–C). Notably, our SDM experiments highlight the contributions of these groups in contrast to the nonspecific and nonpolar interactions of the narrow pocket. In HY11-6B2, the $Glu95Gln_{HC}$ mutant showed increased K_D, specifically through K_{off}; no change in K_{on} was observed, suggesting that a strong complementary charge is necessary to retain the ligand (Figure S5A). The double mutant $Glu95Gln_{HC}/Gln89Ala_{LC}$ ablated binding despite retaining a hydrogen-bonding capable residue. Both mutations were tolerated individually, suggesting that this change is attributable to a lack of sufficient electrostatic charge. This builds on previous work detailing the key conserved binding motif, the electrostatic interaction between a ligand amine and a complementary charged residue.[13−15,22] Re-introduction of the murine framework residue $Tyr36_{LC}$ showed increased binding compared to variants where $Phe36_{LC}$ was present (Table 3), supporting the requirement for strong electrostatic networks. As a framework residue, $Tyr36_{LC}$ was initially not considered important for ligand binding, an oversight that we could not have corrected without structural data. This highlights the importance of structural information and the role of framework residues in interactions.

Some fentanyl-binding mAbs share the same pocket design, with a key glutamic acid, as the HY11-7E1 family, such as FenAb-208 and 609,[15] and perhaps P1C3H9.[32] Eubanks et al.[24] described a deep pocket that utilizes a glutamic acid for fentanyl binding but with the fentanyl inverted and the phenethyl-ring pointing into the pocket. Ligand orientation and potential affinity and efficacy are a direct consequence of hapten design. In the above mAbs, the site of linker attachment is exiting the binding pocket; the linker position often determines which functional groups are pointing into the binding pocket and available for interactions with critical residues. As all three studies report similar highest affinities, it is possible that a limit of affinity is being reached as well. Unlike proteins, small ligands have limited functional groups available for binding. Fentanyl has three available heteroatoms; carfentanil has five. Often, only 2−3 heteroatoms are coordinated during mAb binding;[14,15,22] Eubanks et al.[24] shows only one heteroatom coordinated. While other FAs display many more heteroatoms or functional groups,[30] it is not clear whether strong coordination of all of these is necessary or effective at improving binding. For the mAbs described here, the K_D of mutants largely depended on changes in K_{off}, while K_{on} changes were small. When we reintroduced $Tyr36_{LC}$ into 7E1_Hu (DE), we saw an ∼1000-fold decrease in K_{off} when binding carfentanil or fentanyl and an ∼10-fold decrease in K_{on} for carfentanil (Figure S5B). This engineered mAb showed restored affinity to fentanyl and carfentanil, similar to parental 7E1_Mu and 5B1_Mu, respectively, but did not surpass either. Eubanks et al.[24] reported cross-reactive binding to eight FAs that have a conserved apical phenethyl ring. They report a similar K_D but an inverted K_{on} and K_{off} relation (a K_D dependent on K_{on} changes with a constant K_{off}) using a competitive SPR method and a lower CSA than mAbs

https://doi.org/10.1021/acsomega.4c06617
ACS Omega 2024, 9, 42506−42519

reported here. Ligand CSA was reduced by ∼75 Å^2 in fentanyl binders and ∼95 Å^2 in carfentanil binders,[24] compared to 7E1_Mu and 7E1_Hu (DE), respectively. Despite these differences, optimal mAb affinities appear to be achievable through the coordination of a few conserved polar atoms. However, the impact of these differences in binding modality and kinetics on *in vivo* pharmacokinetics requires further investigation when considering rational mAb design.

While strong functional group coordination is essential, to ensure specificity to F/FA, these deep pockets must also accommodate various additional functional groups. Our structural comparison showed that 7E1 and 5B1 mAbs share a mobile CDRH3, which is flexible enough to accommodate ligand binding while retaining a low K_{off}. 5B1 has an even greater CDRH3 flexibility, which is highlighted in the Apo structure (Figure 4C). Previous studies on opioid-binding crystal structures have reported low electron density for highly mobile CDRs due to the flexibility preventing well-ordered packing.[24] We observed this in 5B1, but not in 7E1, as CDRH3 adopted a β-sheet conformation in the 7E1_Hu (DE) Apo structure, although this β-sheet rigidity reduces following fentanyl binding. Focusing on the 7E1 CRDH3, we see that not only is CDRH3 engagement distinct between ligands but also the rotation of the ligand is shifted (∼30°) between fentanyl and carfentanil, possibly to prevent clashing between the ester group and $Tyr91_{LC}$ (Figure 3C,E). Despite this shift, the key bonds at $Gln89_{LC}$ and $Glu95_{HC}$ are retained. Furthermore, the more open "foreground" of 7E1_Hu (DE) helps accommodate additional functional groups, where we see the ester group of carfentanil protruding (Figure 3C).

Overall, as our previous work[22] and others[15] have discussed, deep-pocketed mAbs such as those described here have some considerations in terms of mAb specificity for small-molecule targets. Notably, deeper-pocketed mAbs may have therapeutic benefits over more open binding sites because they may prevent nonspecific binding to off-target molecules or proteins. However, this becomes a balancing act with F/FA and NPS; that is, can broad specificity to illicit targets of interest be engineered into existing mAbs while limiting off-target impacts? We believe the answer is yes when structural information can be leveraged to make more informed mutagenesis decisions. Rapidly advancing machine learning and *in silico* modeling techniques can accelerate therapeutic development. However, with such methods, strong base structural knowledge and how it relates to pharmacological activity are still necessary to avoid erroneous leads. Similar antibody engineering strategies could be applied to mAbs against other drug targets, nerve agents, poisons, and chemical threats.

METHODS

Animals. All experiments were approved by the University of Minnesota Institutional Animal Care and Use Committee prior to initiation. Balb/c mice (Envigo) were 8−10 weeks on arrival, and a 1 week habituation period was allowed prior to the initiation of experiments. Mice were housed in groups of 4 under a 14/10 light/dark cycle, with with food and water provided *ad libitum*. All behavioral assessments occurred during the light cycle, and mice were acclimated to the testing room for 1 h prior to experimentation.

Isolation and Expression of mAbs. HY6-F9 was previously isolated from mice immunized with F_1-sKLH on days 0 and 28.[21] HY11-6B2 and HY11-7E1 were previously isolated from mice immunized with F_1-CRM once, and splenocytes were collected early on day 18 due to COVID19-related work interruptions.[20] For isolation of novel mAbs HY17-19, mice were immunized with F_1-CRM or F_{13}-CRM on days 0 and 28 as indicated. Vaccines were formulated in alum adjuvant (InvivoGen, Alhydrogel 2%) and injected intramuscularly with a 30 μL/site injection volume. Blood samples were collected on days 14 and 32 to assess serum titer by ELISA. Splenocytes were collected on day 32, and hybridoma fusion was performed with the ClonaCell-HY kit according to the manufacturer's instructions (Stemcell Cat # 03800). For the *in vivo* challenge shown in Figure 1, HY6-F9 and HY11-7E1 were murine mAbs expressed from hybridoma and purified by Protein A chromatography. For the *in vivo* challenge in Figure 3, HY17-19 chimeric mAbs were expressed using the ExpiCHO expression system (Thermo Fisher Cat # A29133).

***In Vivo* Opioid Challenge.** Male Balb/c mice were passively immunized with 40 mg/kg mAb. Twenty-four hours later, mice were challenged with s.c. fentanyl 0.1 mg/kg, acetylfentanyl 1.0 mg/kg, carfentanil 0.02 mg/kg, or with a mixture of fentanyl and carfentanil as indicated. Opioid-induced antinociception was measured 30 min after administration as latency to respond on a hot plate (Columbus Instruments) set to 54 °C with a maximum cutoff of 60 s. A lift or flick of a hind paw was considered a response, and mice were removed from the plate immediately if a response was recorded. Opioid-induced respiratory depression and bradycardia were measured with a MouseOx Plus pulse oximeter (Starr Life Sciences), which uses an infrared sensor attached to a collar clip. Immediately after behavior measurements, mice were euthanized, and serum and brain tissues were collected for analysis by LCMS as described.[17]

Generation of Point Mutants. Double-stranded DNA fragments containing desired mutations were generated with 20 base pair overlaps to backbone vectors on each end (IDT, Coralville, IA). Vectors were prepared using Gibson assembly, and mAbs were expressed using paired HC and LC vectors using the ExpiCHO expression system. Antibody engineering experiments involving r/sNA were approved by the UMN and UW Institutional Biosafety Committees.

Determination of mAb Affinity. Biolayer interferometry (BLI) was performed by using an Octet R8 system (Sartorius). Biotinylated haptens F_1 and F_{11} were loaded on a streptavidin-coated biosensor (Sartorius, Cat # 18-5019) in PBS buffer + 0.05% Tween-20 (PBS-T, Thermo Fisher Cat # 28352). The biotinylated haptens were loaded at 0.05 μg/mL and 0.2 μg/mL (biotinylated F_1) or 0.1 μg/mL and 0.3 μg/mL (biotinylated F_{11}) for 60 s. The mAb samples were measured at 10, 20, and 40 nM to obtain full binding curves. Baselines were measured for 60 s, and association and dissociation were recorded for 5 and 10 min, respectively. Competitive ELISA was performed as described[20] using F_1-BSA or F_{13}-BSA as the coating antigen on 96-well flat-bottom microplates (Corning, Cat # 9018) overnight. The plates were then blocked with 1% gelatin in PBS-T to reduce nonspecific binding. Subsequently, the plates were incubated with mAbs at 7.8 ng/mL and competitors, from 0.01 M to 0.1 pM, for 2 h. Plates were washed and incubated with HRP-labeled secondary antibodies, and colorimetric signals were generated with SigmaFast OPD substrate (Sigma, Cat # P9187) and quantitated on a Victor Nivo Multimode Plate Reader (PerkinElmer).

https://doi.org/10.1021/acsomega.4c06617
ACS Omega 2024, 9, 42506−42519

Generation of 6xHis-Fab Expression Vectors. The VH region of each mAb was PCR-amplified from pcDNA3.4 plasmid DNA, and the Platinum SuperFi II PCR Master Mix was used to linearize a PMN destination backbone with a generic human CH1 region, a C-terminal 6xHis-tag, and an N-terminal secretion tag. The VH region was cloned into the linearized backbone using the Infusion HD Cloning Plus kit (Takara Bio, Cat # 639650) with optimal primers generated by the Takara Bio primer design tool. The chimeric His-Fab expression vectors were then transformed into NEB5α *E. coli* cells (New England BioLabs, Cat # C2987H), and DNA was isolated using a MidiPrep kit (Qiagen, Cat # 12945). Sequencing of expression vectors was performed by a Genewiz.

Expression of 6xHis-Fab Constructs. All His-Fabs were expressed via transient expression in HEK293e cells. Transfection reagents were prepared with 2 mL of PEI at 1 mg/mL, 250 μg of each VH-6xHis and VL plasmid constructs, and 38 mL of PBS per liter of planned transfection culture. Cells were transfected at 1×10^6 cells/mL, and the culture was incubated at 37 °C with 5% CO_2 and shaking at 140 rpm for 6 days prior to harvest.

SEC Purification and Preparation of Fabs for Crystallization. Following benchtop purification with a nickel affinity column, Fabs were concentrated to 2 mL using a 10 kDa Amicon centrifugal filter (Millipore Sigma, Cat # UFC801024) and sterile-filtered using an Ultra-Free-CL (Millipore Sigma, Cat # UFC40GV25). The Fabs were then injected onto a Superdex 200 16/600 size-exclusion column (Cytiva) equilibrated with 5 mM HEPES buffer, pH 7.5, and 150 mM NaCl using an AKTApure (GE Biosciences) system. Fab peak fractions were pooled and concentrated again (Amicon, Millipore Sigma) for crystallization trials.

Crystallization and Structure Determination. Fabs were incubated with a twofold molar excess of their target ligand for >2 h at 23 °C prior to crystallization trials. For 7E1_Hu (DE):F_{11}, we incubated Fabs with the F_{11} carfentanil-based hapten. This hapten is chemically identical to F_{13} (in F_{13}-CRM vaccine) when considering bound functional groups. The difference between the two occurs distal to the ethyl group linker. Conditions from commercial 96-well screens were used with Swissci MRC 2 Well UVXPO plates (Molecular Diensions, Cat # MD11-00-40) and set using an NT8 drop setter (Formulatrix). Commercial 96-well screens used include MCSG-1−3 (Microlytic, Cat # MCSG-1, MCSG-2, MCSG-3), Xtal High Throughput and Additive Screen (Hampton Research, Cat # HR2-428), and WPS2 (Rigaku, Cat # 1010673). Optimization of crystallization conditions was performed in EASYXTAL 15-well crystallization trays (NextalBiotech, Cat # 132008). The final conditions that produced a diffracting crystal are listed as follows.

All conditions were optimized with a protein-to-mother liquor ratio of 1:1, in 0.5 μL:0.5 μL amounts. 6B2_Mu:fentanyl (25 mg/mL) was crystallized with 25% PEG 3350 (Hampton Research, Cat # 1008054), 0.24 M ammonium sulfate, 0.1 M Bis-Tris (pH 5.5), and 0.01 M $NiCl_2$. 7E1_Mu:fentanyl (25 mg/mL) was crystallized with 1.4 M ammonium sulfate, 0.1 M MES (pH 6.5), and 0.01 M $CoCl_2$. 7E1_Hu (DE) Apo (21.88 mg/mL) was crystallized with 25% PEG 4000 (Hampton Research, Cat # 1008058), 0.1 M sodium acetate (pH 4.6), and 0.2 M ammonium sulfate. 7E1_Hu (DE):F_{11} (20 mg/mL) was crystallized with 2.0 M ammonium sulfate and 0.1 M sodium acetate (pH 4.6). 5B1_Mu Apo (20 mg/mL) was crystallized with 27% PEG 8000 (Hampton Research, Cat # 1008062), 0.02 M $CoCl_2$, and 0.15 M ammonium sulfate. 5B1_Mu:fentanyl (20 mg/mL) was crystallized with 25% PEG 3350 (Hampton Research, Cat # 1008054), 0.2 M ammonium sulfate, and 0.1 M Bis-Tris (pH 5.5).

Crystals were flash-cooled in their crystallizing condition buffered with 30% ethylene glycol (HY11-6B2_Mu:fentanyl) and 30% glycerol (HY18-5B1_Mu Apo) or transferred to Parabar 10312 (Hampton Research, Cat # HR2-862) (HY11-7E1_Hu (DE) Apo, HY11-7E1_Hu (DE):F_{11}, HY18-5B1_Mu:fentanyl). Data were collected at either Sector 19 at the Advanced Photon Source (Argonne National Laboratories) or Beamline 5.0.1 at the Advanced Light Source (Lawrence Berkeley National Lab) and then processed with either XDS[35] or HKL-2000.[36] Data were reduced using CCP4i2,[37] and then, structures were phased and solved using the Phenix software suite,[38] the *Coot* toolkit,[39] and ChimeraX[40] with the ISOLDE[41] plug-in. The 6B2_Mu:fentanyl crystal displayed high (∼50%) tNCS and is further discussed in Figure S2. 7E1_Mu:fentanyl produced small crystals prone to radiation damage. Due to this, three data sets were collected from three separate crystals isolated from the same well and merged in HKL-2000. The 5B1_Mu:fentanyl crystal was merohedrally twinned, so the twin law -k,-h,-l was used during refinement in the Phenix software suite. Structure visualizations, comparisons, and molecular representations were created in ChimeraX.[40] CSA calculations were performed in dr_sasa.[42] All collection and refinement data are listed in Table 2.

Statistical Analysis and Software. Statistical analysis for *in vivo* experiments and competitive ELISA was performed using GraphPad Prism v9.2. For determination of *in vivo* mAb efficacy, differences in the distribution of opioids in the brain and serum were analyzed by one-way ANOVA with Dunnett's multiple comparisons test. For competitive ELISA, the IC_{50} was determined by four-parameter logistic regression. For BLI experiments, the calculation of the results, including K_{on}, K_{off}, and K_D and the fitness of the curve, was performed by Octet analysis software (Sartorius). Figure 2A was generated in ChemSketch, and Figure 2F was generated in BioRender.

■ ASSOCIATED CONTENT

Data Availability Statement

All crystallographic data sets have been deposited in the Protein Data Bank and are publicly available as of the date of publication. Accession numbers are listed as follows: 9AXN, 9AXO, 9AXP, 9AXQ, 9AXR, 9AXS. This paper does not report original code or other original data. Any additional information required to reanalyze the data reported in this paper is available from the lead contact upon request.

Supporting Information

The Supporting Information is available free of charge at https://pubs.acs.org/doi/10.1021/acsomega.4c06617.

> Opioid-induced bradycardia, respiratory depression, and antinociception; table depicting CDRs of lead mAbs; image of 6B2_Mu crystal packing with tNCS; 7E1 apo structure with F_{11} and modeled carfentanil; and BLI traces comparing off-rates of mutant mAbs (PDF)

■ AUTHOR INFORMATION

Corresponding Authors

Marie Pancera − *Vaccine and Infectious Disease Division, Fred Hutchinson Cancer Center, Seattle, Washington 98109, United States*; Email: mpancera@fredhutch.org

https://doi.org/10.1021/acsomega.4c06617
ACS Omega 2024, 9, 42506−42519

Marco Pravetoni − *Department of Psychiatry and Behavioral Sciences, School of Medicine, University of Washington, Seattle, Washington 98195, United States; Center for Medication Development for Substance Use Disorders and Overdose, University of Washington, Seattle, Washington 98195, United States*; Email: mprave@uw.edu

Authors

Justas Rodarte − *Vaccine and Infectious Disease Division, Fred Hutchinson Cancer Center, Seattle, Washington 98109, United States*

Carly Baehr − *Department of Pharmacology, University of Minnesota Medical School, Minneapolis, Minnesota 55455, United States*; orcid.org/0000-0002-3395-6776

Dustin Hicks − *Department of Pharmacology, University of Minnesota Medical School, Minneapolis, Minnesota 55455, United States*

Morgan McGovern − *Vaccine and Infectious Disease Division, Fred Hutchinson Cancer Center, Seattle, Washington 98109, United States*

Yue Zhang − *Department of Pharmacology, University of Minnesota Medical School, Minneapolis, Minnesota 55455, United States; Department of Psychiatry and Behavioral Sciences, School of Medicine, University of Washington, Seattle, Washington 98195, United States*

Pedro Silva-Ortiz − *Department of Pharmacology, University of Minnesota Medical School, Minneapolis, Minnesota 55455, United States*

Bryan Hannon − *Vaccine and Infectious Disease Division, Fred Hutchinson Cancer Center, Seattle, Washington 98109, United States; Department of Psychiatry and Behavioral Sciences, School of Medicine, University of Washington, Seattle, Washington 98195, United States*

Sowmya Duddu − *Vaccine and Infectious Disease Division, Fred Hutchinson Cancer Center, Seattle, Washington 98109, United States*

Complete contact information is available at: https://pubs.acs.org/10.1021/acsomega.4c06617

Author Contributions

[⊥]J.R. and C.B. contributed equally to this work. M. Pancera and M. Pravetoni supervised the study. C.B. isolated HY17-19 mAbs and designed and performed *in vivo* efficacy experiments, P.S.O. performed the HY17-19 *in vivo* experiments. J.R., M.M., B.H., and S.D. performed mAb expression, complex preparation, and crystallographic data collection; J.R., M.M., and B.H. solved the structures and performed further analyses. D.H. and Y.Z. performed mAb expression and *in vitro* binding assays. The manuscript was written by J.R., C.B., D.H., and M.M.; the manuscript was reviewed and edited by all authors.

Notes

The authors declare the following competing financial interest(s): Authors M.Pa., J.R., M.M., Y.Z., P.S.O., B.H., and S.D. declare no competing interests. M.Pr., C.B., and D.H. are co-inventors of patent applications describing mAbs against fentanyl and carfentanil included in this manuscript. M.Pr. is the founder and shareholder of CounterX Therapeutics, Inc. Plasmids for expression of reported antibodies are available upon request to the lead contact. Haptens, either biotinylated or sKLH conjugated, are available upon request; please direct inquiries to Marco Pravetoni. All materials are subject to standard MTA agreements and IP restrictions where applicable.

■ ACKNOWLEDGMENTS

Research reported in this publication was supported by a HEAL Administrative Supplement to grant UG3 DA047711 and by grants UG3 DA057850 and U01 DA051658 from the NIH, National Institute on Drug Abuse (NIDA), National Institute of Neurological Disorders and Stroke (NINDS), and the CounterACT program. The authors thank the Garvey Family and the UW Garvey Institute for Brain Solutions for the generous Rick L. Seaver Endowed Professorship in Brain Wellness to M. Pravetoni. The authors are particularly grateful to L. Stamatatos for the use of laboratory space and equipment. The authors thank the J. B. Pendleton Charitable Trust for its generous support of Formulatrix robotic instruments. X-ray diffraction data was collected at the Berkeley Center for Structural Biology, which is supported in part by the Howard Hughes Medical Institute. The Advanced Light Source is a Department of Energy Office of Science User Facility under Contract No. DE-AC02-05CH11231. The Pilatus detector on 5.0.1. was funded by NIH grant S10OD021832. The ALS-ENABLE beamlines are supported in part by the National Institutes of Health and the National Institute of General Medical Sciences, grant P30 GM124169. Some results shown in this report are derived from work performed at Argonne National Laboratory (ANL), Structural Biology Center (SBC) at the Advanced Photon Source (APS), under U.S. Department of Energy, Office of Biological and Environmental Research contract DE-AC02-06CH11357.

■ REFERENCES

(1) Ghose, R.; Forati, A. M.; Mantsch, J. R. Impact of the COVID-19 Pandemic on Opioid Overdose Deaths: a Spatiotemporal Analysis. *J. Urban Health* **2022**, *99*, 316−327.

(2) Jones, C. M.; Shoff, C.; Hodges, K.; et al. Receipt of Telehealth Services, Receipt and Retention of Medications for Opioid Use Disorder, and Medically Treated Overdose Among Medicare Beneficiaries Before and During the COVID-19 Pandemic. *JAMA Psychiatry* **2022**, *79*, 981−992.

(3) Mattocks, K. M.; Moore, D. T.; Wischik, D. L.; Lazar, C. M.; Rosen, M. I. Understanding opportunities and challenges with telemedicine-delivered buprenorphine during the COVID-19 pandemic. *J. Substance Abuse Treat.* **2022**, *139*, No. 108777.

(4) Ahmad, F. B.; Rossen, L. M.; Sutton, P.; Cisewski, J. A. National Center for Health Statistics 2023 https://www.cdc.gov/nchs/nvss/vsrr/drug-overdose-data.htm.

(5) Tanz, L. J.; Gladden, R. M.; Dinwiddie, A. T.; et al. Routes of Drug Use Among Drug Overdose Deaths — United States, 2020−2022. *MMWR, Morb. Mortal. Wkly. Rep.* **2024**, *73*, 124−130.

(6) Abbas, B.; Marotta, P. L.; Goddard-Eckrich, D.; et al. Socio-ecological and pharmacy-level factors associated with naloxone stocking at standing-order naloxone pharmacies in New York City. *Drug Alcohol Depend.* **2021**, *218*, No. 108388.

(7) Khan, M. R.; Hoff, L.; Elliott, L.; et al. Racial/ethnic disparities in opioid overdose prevention: comparison of the naloxone care cascade in White, Latinx, and Black people who use opioids in New York City. *Harm Reduction J.* **2023**, *20*, No. 24, DOI: 10.1186/s12954-023-00736-7.

(8) Noble, F.; Marie, N. Management of Opioid Addiction With Opioid Substitution Treatments: Beyond Methadone and Buprenorphine. *Front Psychiatry* **2019**, *9*, 742.

(9) Joudrey, P. J.; Adams, Z. M.; Bach, P.; et al. Methadone Access for Opioid Use Disorder During the COVID-19 Pandemic Within the United States and Canada. *JAMA Network Open* **2021**, *4*, No. e18223.

(10) Compton, W. M.; Volkow, N. D. Extended-Release Buprenorphine and Its Evaluation With Patient-Reported Outcomes. *JAMA Network Open* **2021**, *4*, No. e219708.

(11) Moss, R. B.; Carlo, D. J.Higher Doses of Naloxone are Needed in the Synthetic Opiod Era. In *Substance Abuse: Treatment, Prevention, and Policy*; Wiley, 2019; Vol. *14*, pp 1−6.
(12) United Nations. World Drug Report 2023 https://www.unodc.org/unodc/en/data-and-analysis/world-drug-report-.html.
(13) Tars, K.; Kotelovica, S.; Lipowsky, G.; et al. Different binding modes of free and carrier-protein-coupled nicotine in a human monoclonal antibody. *J. Mol. Biol.* **2012**, *415*, 118−127.
(14) Pozharski, E.et al. *Molecular Biology*; Academic Press, 2004; Vol. *337*, pp 691−697.
(15) Triller, G.; Vlachou, E. P.; Hashemi, H.; et al. A trypanosome-derived immunotherapeutics platform elicits potent high-affinity antibodies, negating the effects of the synthetic opioid fentanyl. *Cell Rep.* **2023**, *42*, No. 112049.
(16) Robinson, C.; Gradinati, V.; Hamid, F.; et al. Therapeutic and Prophylactic Vaccines to Counteract Fentanyl Use Disorders and Toxicity. *J. Med. Chem.* **2020**, *63*, 14647−14667.
(17) Baehr, C.; Robinson, C.; Kassick, A.; et al. Preclinical Efficacy and Selectivity of Vaccines Targeting Fentanyl, Alfentanil, Sufentanil, and Acetylfentanyl in Rats. *ACS Omega* **2022**, *7*, 16584−16592.
(18) Crouse, B.; Wu, M. M.; Gradinati, V.; et al. Efficacy and Selectivity of Monovalent and Bivalent Vaccination Strategies to Protect against Exposure to Carfentanil, Fentanyl, and Their Mixtures in Rats. *ACS Pharmacol. Transl. Sci.* **2022**, *5*, 331−343.
(19) Crouse, B.; Miller, S. M.; Muelken, P.; et al. A TLR7/8 agonist increases efficacy of anti-fentanyl vaccines in rodent and porcine models. *npj Vaccines* **2023**, *8*, No. 107, DOI: 10.1038/s41541-023-00697-9.
(20) Hicks, D.; Baehr, C.; Silva-Ortiz, P.; et al. Advancing humanized monoclonal antibody for counteracting fentanyl toxicity towards clinical development. *Hum. Vaccines Immunother.* **2022**, *18*, No. 2122507.
(21) Baehr, C.; Kelcher, A. H.; Khaimraj, A.; et al. Monoclonal antibodies counteract opioid-induced behavioral and toxic effects in mice and rats. *J. Pharmacol. Exp. Ther.* **2020**, *375*, 469−477.
(22) Rodarte, J. V.; Baehr, C.; Hicks, D.; et al. Structures of drug-specific monoclonal antibodies bound to opioids and nicotine reveal a common mode of binding. *Structure* **2023**, *31*, 20−32.
(23) Wu, T. T.; Kabat, E. A. An analysis of the sequences of the variable regions of Bence Jones proteins and myeloma light chains and their implications for antibody complementarity. *J. Exp. Med.* **1970**, *132*, 211−250.
(24) Eubanks, L. M.; Pholcharee, T.; Oyen, D.; et al. An Engineered Human-Antibody Fragment with Fentanyl Pan-Specificity That Reverses Carfentanil-Induced Respiratory Depression. *ACS Chem. Neurosci.* **2023**, *14*, 2849−2856.
(25) Vo, Q. N.; Mahinthichaichan, P.; Shen, J.; Ellis, C. R. How μ-opioid receptor recognizes fentanyl. *Nat. Commun.* **2021**, *12*, No. 984, DOI: 10.1038/s41467-021-21262-9.
(26) Bick, M. J.; Greisen, P. J.; Morey, K. J.; et al. Computational design of environmental sensors for the potent opioid fentanyl. *eLife* **2017**, *6*, No. e28909, DOI: 10.7554/eLife.28909.
(27) Kurczab, R.; Sliwa, P.; Rataj, K.; Kafel, R.; Bojarski, A. J. Salt Bridge in Ligand-Protein Complexes-Systematic Theoretical and Statistical Investigations. *J. Chem. Inf. Model.* **2018**, *58*, 2224−2238.
(28) Baehr, C. A.; Wu, M. M.; Pandit, S. G.; et al. Pharmacological Profiling of Antifentanyl Monoclonal Antibodies in Combination with Naloxone in Pre- and Postexposure Models of Fentanyl Toxicity. *J. Pharmacol. Exp. Ther.* **2022**, *381*, 129−136.
(29) Bremer, P. T.; Burke, E. L.; Barrett, A. C.; Desai, R. I. Investigation of monoclonal antibody CSX-1004 for fentanyl overdose. *Nat. Commun.* **2023**, *14*, No. 7700.
(30) Ringuette, A. E.; Spock, M.; Lindsley, C. W.; Bender, A. M. DARK Classics in Chemical Neuroscience: Carfentanil. *ACS Chem. Neurosci.* **2020**, *11*, 3955−3967.
(31) Chen, X. Y.; Wang, L.; Ma, X.; et al. Development of fentanyl-specific monoclonal antibody (mAb) to antagonize the pharmacological effects of fentanyl. *Toxicol. Appl. Pharmacol.* **2024**, *486*, No. 116918.
(32) Ban, B.; Barrientos, R. C.; Oertel, T.; et al. Novel chimeric monoclonal antibodies that block fentanyl effects and alter fentanyl biodistribution in mice. *mAbs* **2021**, *13*, No. 1991552, DOI: 10.1080/19420862.2021.1991552.
(33) Smith, L. C.; Bremer, P. T.; Hwang, C. S.; et al. Monoclonal Antibodies for Combating Synthetic Opioid Intoxication. *J. Am. Chem. Soc.* **2019**, *141*, 10489−10503.
(34) Urban, K.; Gkeka, A.; Chandra, M.; et al. The fentanyl-specific antibody FenAb024 can shield against carfentanil effects. *Toxicol. Lett.* **2024**, *396*, 1−10.
(35) Kabsch, W. XDS. *Acta Crystallogr., Sect. D* **2010**, *66*, 125−132.
(36) Otwinowski, Z.; Minor, W. Processing of X-ray diffraction data collected in oscillation mode. *Methods Enzymol.* **1997**, *276*, 307−326, DOI: 10.1016/S0076-6879(97)76066-X.
(37) Potterton, L.; Agirre, J.; Ballard, C.; et al. CCP4i2: the new graphical user interface to the CCP4 program suite. *Acta Crystallogr., Sect. D* **2018**, *74*, 68−84.
(38) Liebschner, D.; Afonine, P. V.; Baker, M. L.; et al. Macromolecular structure determination using X-rays, neutrons and electrons: recent developments in Phenix. *Acta Crystallogr., Sect, D* **2019**, *75*, 861−877.
(39) Emsley, P.; Lohkamp, B.; Scott, W. G.; Cowtan, K. Features and development of Coot. *Acta Crystallogr., Sect. D* **2010**, *66*, 486−501.
(40) Pettersen, E. F.; Goddard, T. D.; Huang, C. C.; et al. UCSF ChimeraX: Structure visualization for researchers, educators, and developers. *Protein Sci.* **2021**, *30*, 70−82.
(41) Croll, T. I. ISOLDE: a physically realistic environment for model building into low-resolution electron-density maps. *Acta Crystallogr., Sect. D* **2018**, *74*, 519−530.
(42) Ribeiro, J.; Rios-Vera, C.; Melo, F.; Schuller, A. Calculation of accurate interatomic contact surface areas for the quantitative analysis of non-bonded molecular interactions. *Bioinformatics* **2019**, *35*, 3499−3501.

https://doi.org/10.1021/acsomega.4c06617
ACS Omega 2024, 9, 42506−42519